Hyperspectral Imaging for Dermal Hemoglobin Spectroscopy

by

Peter J. Dwyer
Wellman Laboratories of Photomedicine
Massachusetts General Hospital
50 Blossom Street
Bartlett Extension Building
Boston, Massachusetts 02114
and
Charles A. DiMarzio
Center for Electromagnetics Research
Northeastern University
Boston, Massachusetts 02115

ABSTRACT

It has been shown previously that images collected at selected wavelengths in a sufficiently narrow bandwidth can be used to produce maps of the oxygen saturation of hemoglobin in the dermis. A four-wavelength algorithm has been developed based on a two-layer model of the skin, in which the blood is contained in the lower layer (dermis), while the upper layer attenuates some of the reflection and adds a clutter term. In the present work, the algorithm is compared analytically to simpler algorithms using three wavelengths and based on a single-layer model. It is shown through Monte-Carlo models that, for typical skin, the single-layer model is adequate to analyze data from fiber-optical reflectance spectroscopy, but the two-layer model produces better results for imaging systems. Although the model does not address the full complexity of reflectance of a two-layer skin, it has proven to be sufficient to recover the oxygen saturation, and perhaps other medically relevant information. The algorithm is demonstrated on a suction blister, where the epidermis is removed to reveal the underlying dermis. Applications for this imaging modality exist in dermatology, in surgery, and in developing treatment plans for various diseases.

Key Words:. Oxygen saturation, hemoglobin, reflectance spectroscopy.

Part of the SPIE Conference on Subsurface Sensors and Applications
Denver, Colorado • July 1999 SPIE Vol. 3752 • 0277-786X/99/$10.00

1. INTRODUCTION

Fiber–optical reflectometers have been used for tissue spectroscopy to measure the oxygen saturation of hemoglobin *[Knoefel, et. al]*. Performing the same measurement in an imaging format using a CCD camera is attractive because many points can be measured in parallel, the measurement can be done without contact, and it can be done with minimal disturbance, so that, for example, it can be done during surgery without interfering with the surgeon's field of view.

The propagation of light from source to receiver is, however, substantially different from the fiber case, and new models and algorithms are described. In particular, three wavelengths are sufficient for the fiber–based measurements, while at least four are required in the case of a two–layer model of tissue. The expected measurements from the two different types of instruments are shown here, and models and algorithms are compared.

2. REFLECTANCE FROM TISSUE

2.1 Measurement Configurations Several configurations may be conisdered for reflectance measurements, and different results are expected depending upon the configuration. The differences arise from the penetration depth of the light and the differences in collection areas and solid angles.

Total reflectance measurments are made with an integrating sphere. Light is incident on a target area of perhaps a square centimeter or less of tissue, and all the light from a larger area of a few square centimeters around the target is collected, regardless of the angle or location at which it emerges. Thus, the measurement is of the reflected flux divided by the incident flux,

$$R_1 = \frac{\Phi_R}{\Phi_I}.$$

In another type of measurement, the reflectance is measured with a radiometer, which only detects the light in a small solid angle, and from a limited area of the sample. This is also a suitable model for a camera viewing a uniformly illuminated sample. If the area is smaller than the incident beam, this technique determines the scattered radiance, divided by the incident irradiance:

$$R_2 = \frac{L_R(x, y, \theta, \phi)}{E_I},$$

where θ and ϕ are angular coordinates measured from the point of incidence to the radiometer.

If the area of the sample measured by the radiometer is significantly larger than the illuminated area, the technique determines the scattered intensity divided by the incident flux:

$$R_3 = \frac{I_R(\theta, \phi)}{\Phi_I}.$$

In reasonably uniform samples, R_2 and R_3 will be similar, because, over a patch of sample area, dA, $E_I = d\Phi_I/dA$ and $L_R = dI_R/dA$.

In a third configuration, a fiber probe is placed in proximity to the sample. The bifurcated fiber bundle delivers light from a source to the sample *via* one set of fibers, often located in the center of the probe, while the other set collects light from the sample within the core area and acceptance angle of each fiber, and delivers it to the receiver. The reflectance is then a sum over all combinations of receiver and source fibers:

$$R_4 = \frac{\sum_i \sum_j L_{R(ij)(0,0)} \Omega A}{\sum_j \Phi_{I(j)}},$$

where $L_{R(ij)}(0,0)$ is the radiance at normal incidence at the location of receiver fiber i when only source fiber j is illuminated.

2.2 A General Model

Prediction of the behavior of light in a turbid medium has been the subject of many research efforts, both experimental and analytical. The simplest concepts of reflectance can be addressed with the aid of Figure 1. Light entering the medium is scattered along a random path involving many scatterers. Absorption may occur at any point along the path. Finally, some light exits at the measurement point. Absorption and scattering may be characterized by an exponential decrease in flux density with distance along the path, so that for a particular path

$$L_{Rij} = S\, exp\left] - \int_{path[j \to i]} (\mu_s + \mu_a) d\ell \right],$$

where μ_s is the scattering coefficient, μ_a is the absorption coefficient, and S is a constant which characterizes all of the scattering processes involved along the path.

In a general sense, the length of the path will increase with increasing distance between the two points i and j, but it will also depend on the tissue parameters, μ_s and μ_a. On the other hand, for strong scattering, the direction of exiting light will be randomized, leading to a Lambertian reflectivity. Thus, it is anticipated that the reflectance R_2 or R_3, will be representative of the total reflectance R_1. Specifically, $\pi R_3 \approx \pi R_2 \approx R_1$. This reflectivity is, according to several models, the albedo:

$$R_1 = \frac{\mu_s'}{\mu_s' + \mu_a'}.$$

For a two–layer model in which the absorber of interest is entirely in the second layer, we postulate that

$$R = R_0 + T^2 R_1,$$

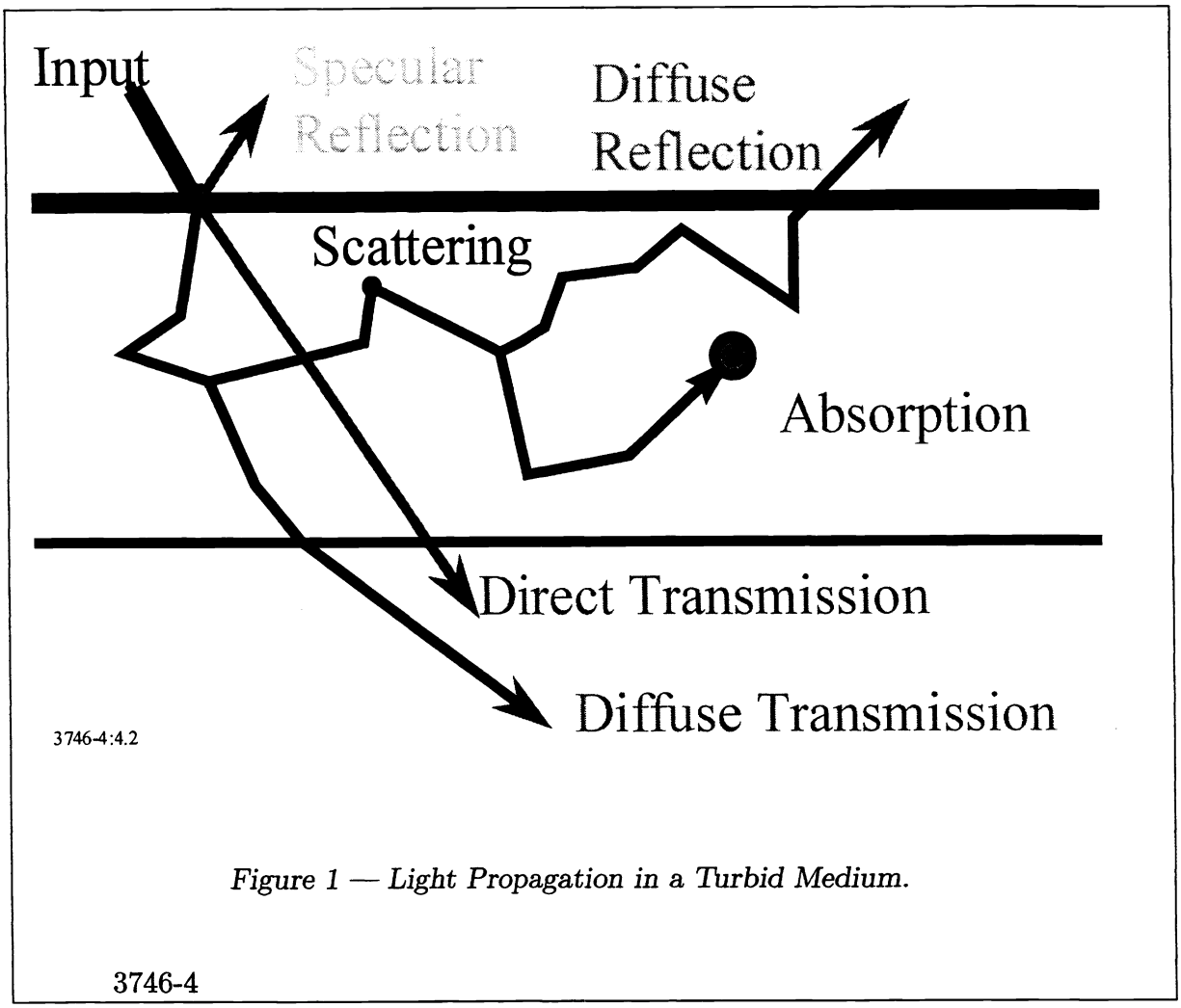

Figure 1 — Light Propagation in a Turbid Medium.

3746-4

where R_0 is the reflectivity of the first layer and T is an empirical constant describing the transmission through that layer. We recognize that this is an approximation, but it provides a more general form than R_1, and we will show that it fits more rigorous theory sufficiently to result in good measuremments of oxygen saturation.

2.3 Inversion to Determine Blood Oxygen Saturation

The inversion equation to be used depends upon the type of measurement being used. We postulate models where, over a moderate band of wavelengths, the scattering and absorption of bloodless tissue are nearly independent of wavelength. Using a fiber sensor, we assume that there exists an (unknown) effective path length, $\bar{\ell}$, so that

$$R_4 = \bar{S}\, exp - (\mu_s + \mu_a)\bar{\ell}.$$

Then under the above assumptions, with a hemoglobin concentration c and oxygen saturation s,

$$R_4(\lambda) = \bar{S}\, exp - [\mu_s + \mu_{ab} + cs\kappa_o(\lambda) + c(1-s)\kappa_d(\lambda)]\bar{\ell},$$

where $\kappa_o(\lambda)$ and $\kappa_d(\lambda)$ are the absorption coefficients of unit concentrations of oxygenated and deoxygenated hemoglobin respectively, and μ_{ab} is the additional absorption coefficient of other material in the sample.

Inversion can be acheived readily by computing the absorption,

$$A'(\lambda) = log\, \frac{1}{R_4(\lambda)},$$

and noting that

$$A'(\lambda) = log\, \frac{1}{\bar{S}} + \mu_s\bar{\ell} + \mu_{ab}\bar{\ell} + c\bar{\ell}s\kappa_o(\lambda) + c\bar{\ell}(1-s)\kappa_d(\lambda).$$

Defining some new constants,

$$A'(\lambda) = a' + c\bar{\ell}s\kappa_o(\lambda) + c\bar{\ell}(1-s)\kappa_d(\lambda),$$

results in a simple set of three linear equations expressed in matrix form as

$$\begin{pmatrix} A'(\lambda_1) \\ A'(\lambda_2) \\ A'(\lambda_3) \end{pmatrix} = \begin{pmatrix} 1 & \kappa_o(\lambda_1) & \kappa_o(\lambda_1) \\ 1 & \kappa_o(\lambda_2) & \kappa_o(\lambda_2) \\ 1 & \kappa_o(\lambda_3) & \kappa_o(\lambda_3) \end{pmatrix} \begin{pmatrix} a' \\ c\bar{\ell}s \\ c\bar{\ell}(1-s) \end{pmatrix}.$$

This can be written formally as

$$\vec{A'} = \mathcal{M} \begin{pmatrix} \hat{a'} \\ \hat{x} \\ \hat{y} \end{pmatrix},$$

and inverted to determine the unknowns from a set of measured reflectances. The oxygen saturation can then be estimated as

$$\hat{s} = \frac{\hat{x}}{\hat{x} + \hat{y}}.$$

Successful solution is possible when the inverse is defined, namely whenever

$$Det\mathcal{M} \neq 0.$$

With a one fixed wavelength, $\lambda_2 = 586$ nm, and varying λ_1 and λ_2, the determimant of $\mathcal{M}$ has the highest magnitude for wavelengths of 576 and 620 nanometers. These are sufficiently close to 586 nanometers so that the assumption that the other optical parameters are independent of wavelength is valid. The next significant peak is at 570 and 576. We have selected this as the best choice of wavelengths.

For the other types of experiments, the procedure is similar.

$$R_1 = \frac{\mu_s'}{\mu_s' + \mu_a'}$$

leads to

$$A = \frac{1}{R_1} = 1 + \frac{\mu_{ab}}{\mu_s} + \frac{cs}{\mu_s}\kappa_o(\lambda) + \frac{c(1-s)}{\mu_s}\kappa_d(\lambda).$$

Again defining new constants,

$$A = a + bcs\kappa_o(\lambda) + bc(1-s)\kappa_d(\lambda),$$

or

$$\vec{A} = \mathcal{M} \begin{pmatrix} \hat{a} \\ \hat{x} \\ \hat{y} \end{pmatrix},$$

with the same matrix as above.

The only difference between the inversion program for the two experimental configurations is in the definition of A. Specifically, for the fiber sensor we use the apparent absorption, determined from the measured reflectivity, R

$$A'(\lambda) = log\,\frac{1}{R(\lambda)},$$

while for the total–reflectance case we use the inverse of the apparent albedo,

$$A(\lambda) = \frac{1}{R(\lambda)}.$$

Thus, for any measured reflectivity, the two parameters are related by

$$A'(\lambda) = log\, A(\lambda).$$

Expanding the logarithm in Taylor's series,

$$A' \approx A - 1.$$

A four–wavelength algorithm which fits the two–layer model is reported elsewhere *[Dwyer, DiMarzio, and Anderson]*. This model fits

$$R = R_0 + \frac{A}{1 + bcs\kappa_o(\lambda) + bc(1-s)\kappa_d(\lambda)}.$$

4. RESULTS

Figure 2 shows reflectivities predicted by Monte–Carlo calculation *[Jacques and Wang]* as functions of wavelength for three different cases of typical skin; one with the dermis being bloodless, one with a normal concentration of fully oxygenated hemoglobin, and one fully deoxygenated. Figures such as these were completed for each of the models, with concentrations of hemoblobin varying from zero to four times the normal 1.2 mM, and reflectivities were selected at five interesting wavelengths, which are used in our inversion algorithms. For the single–layer model in a radiometer, or camera, geometry, the inverse of the reflectivity is nearly linear in concentration of hemoglobin, as shown in Figure 3, as defined by R_3 earlier. Parameters were obtained from several sources *[Anderson, et. al., Wan, et. al., and Van Gemert, et. al.]*

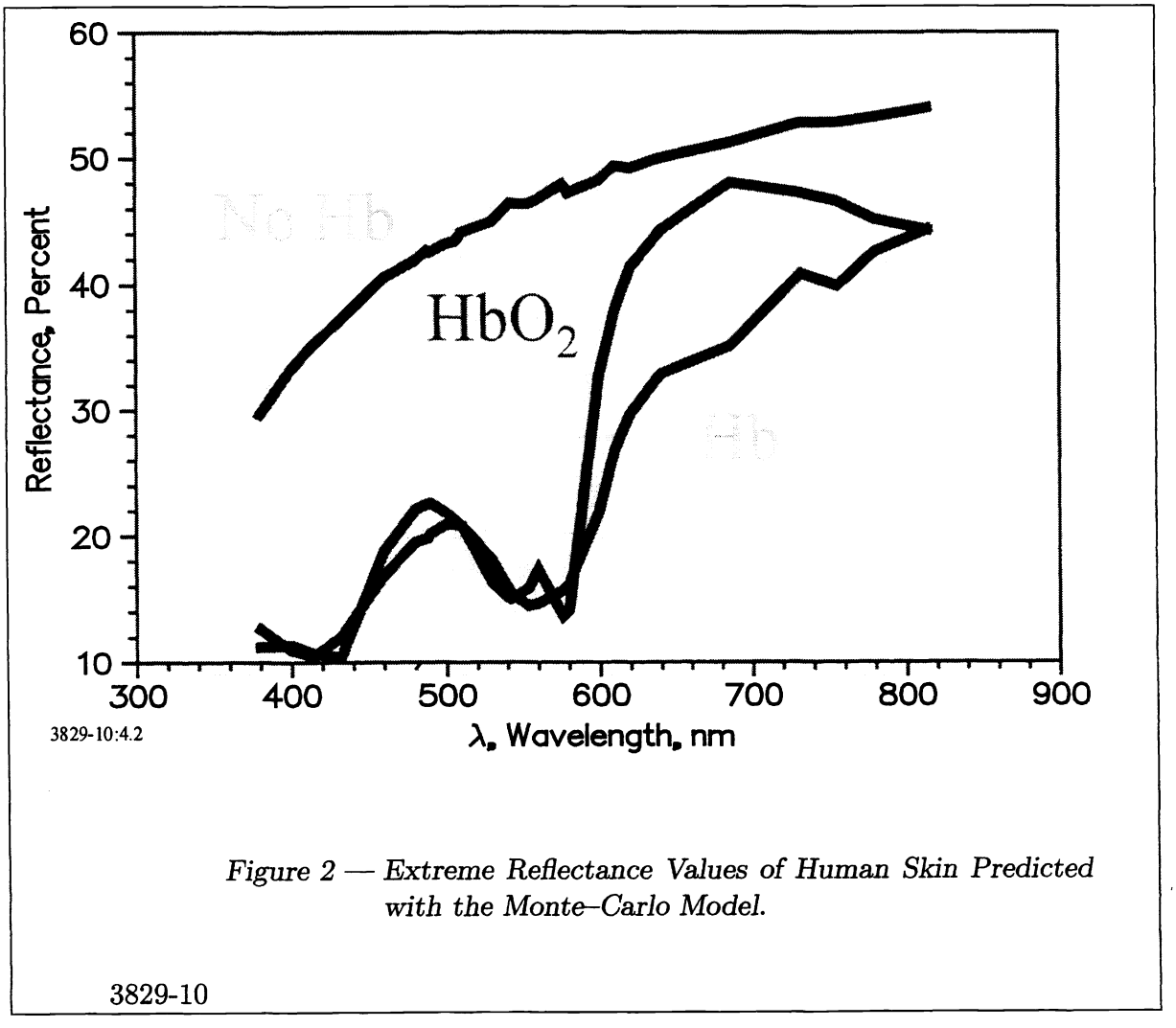

Figure 2 — Extreme Reflectance Values of Human Skin Predicted with the Monte–Carlo Model.

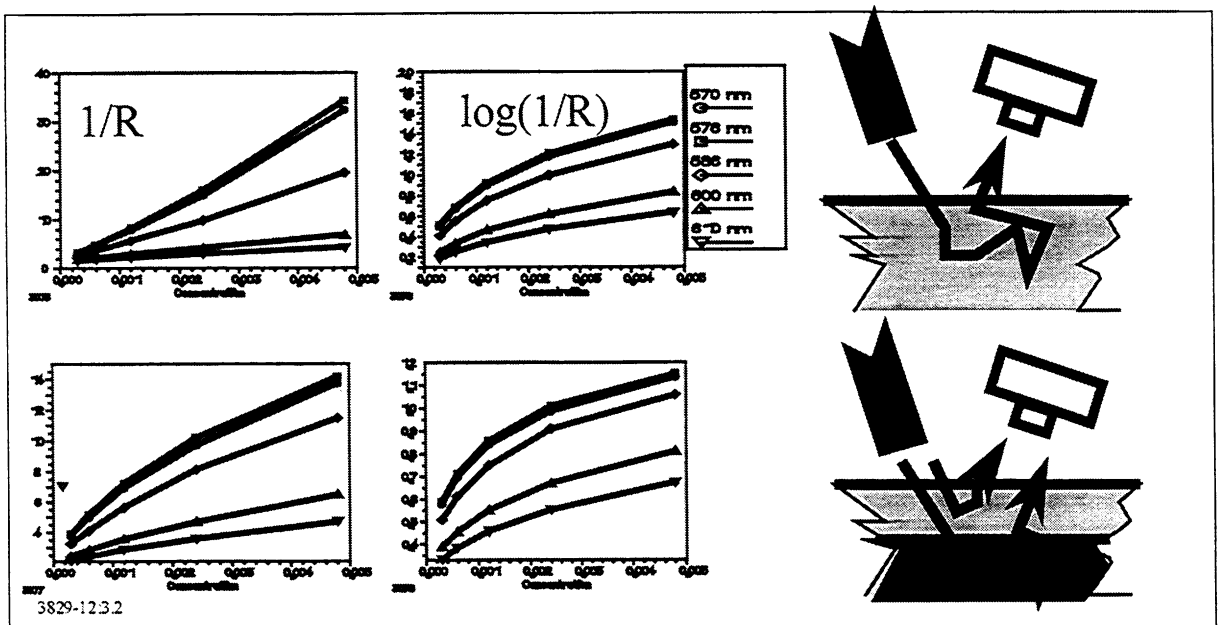

Figure 3 — Comparison of various models to Monte–Carlo Results for Radiometer Geometry.

3829-12

In contrast, for a fiber geometry, following the model of R_4, one expects the logarithm of $1/R$ to be nearly linear in concentration. Furthermore, this is expected to be true in either a two–layer or one–layer model, although the coefficients will, of course, be different. These are consistent with the Monte–Carlo results, as shown in Figure 4.

Next, we compare the results of two different inversion algorithms to the Monte–Carlo model. Figure 5 shows this comparison, for a camera geometry. It is interesting that the four–wavelength algorithm shows better results for both the one and two–layer models. Errors in general are less than 5 percent.

Figure 6 shows a set of images collected and processed using the four–wavelength algorithm. The top row shows the reflectance images. Each one was obtained by dividing an image of the sample by that of a white reference surface. The sample was a suction blister about 1 centimeter in diameter on the subject's forearm. It will be noted that the suction blister is more visible in the shorter wavelengths and that deeper structures such as blood vessels are more evident at the longer wavelengths, as expected. The processed images show the various parameters produced by the algorithm. First, R_0 was postulated to be related to the reflectivity of the epidermis. It approaches zero in the region where the

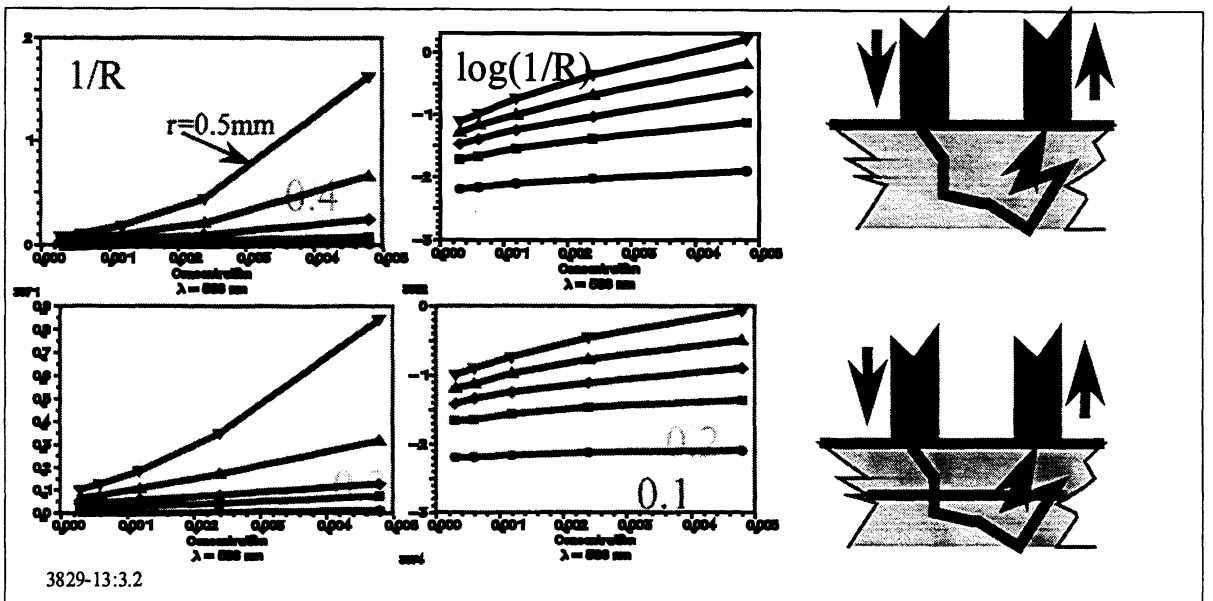

Figure 4 — Comparison of various models to Monte–Carlo Results for Fiber Geometry.

3829-13

epidermis was removed. Second, $1/A$ is related to the transmission through the epidermis and the scattering of the underlying dermis. Note the strong highlights around the edge of the blister and the strong signatures of the deep blood vessels. The third panel shows Bc/A, which is related to the concentration of hemoglobin, and shows a strong increase in the vicinity of the blister as the body begins the healing process. Finally, in the fourth panel, we note that the oxygen saturation of the hemoglobin increases near the injury.

In summary, algorithms for reconstruction of hemoglobin oxygen saturation from reflectivity data must be designed with a knowledge of the details of the specific reflectivity measurement being used. When this is done, useful images can be obtained which not only are quantitatively accurate, but also contain useful spatial information.

7. REFERENCES

Anderson, R.R., Parrish, J.A., "The optics of human skin," *J. Invest. Dermatol.*, 1981 v 77 page 13-19.

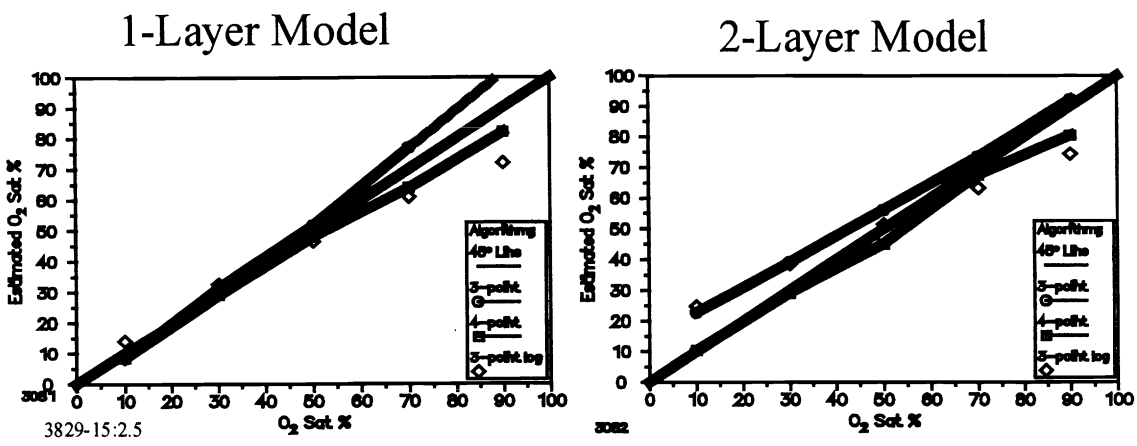

Figure 5 — Comparison of Estimated Oxygen Saturation to that used in the Model.

3829-15

Dwyer, Peter J., Charles A. DiMarzio, and R. Rox Anderson, "Imaging of Blood Oxygenation in Skin Using Four–Wavelength Reflectance Spectroscopy," *Biomedical Sensing, Imaging, and Tracking Technologies II, Proc. SPIE 2976*, SPIE, 1996. Pp. 270–280.

Jacques, Steven L., and Lihong Wang, *Monte Carlo Modeling of Light Transport in Multi– Layered Tissues in Standard C*, M. D. Anderson Cancer Center, University of Texas, 1992, 1993. 178 Pages.

Knoefel, W.T., Kollias, N., Rattner,D.W., Nishioka, N.S., and Warshaw, A.L., "Reflectance Spectroscopy of Pancreatic Microcirculation," *Journal of Applied Physiology*, Jan. 1996. page 116.

Van Gemert, M.J.C., Jacques, Steven L., Sterenborg, H.J.C.M., Star, W.M., "Skin Optics," *IEEE Transactions on Biomedical Engineering*, Dec 1989 v 36 n 12, page 1146.

Wan, S., Anderson, R.R., Parrish, J.A., "Analytical modeling for the optical properties of the skin with in vitro and in vivo applications," *Photochem. Photobiol.*, 1981 v 34 page 493-499.

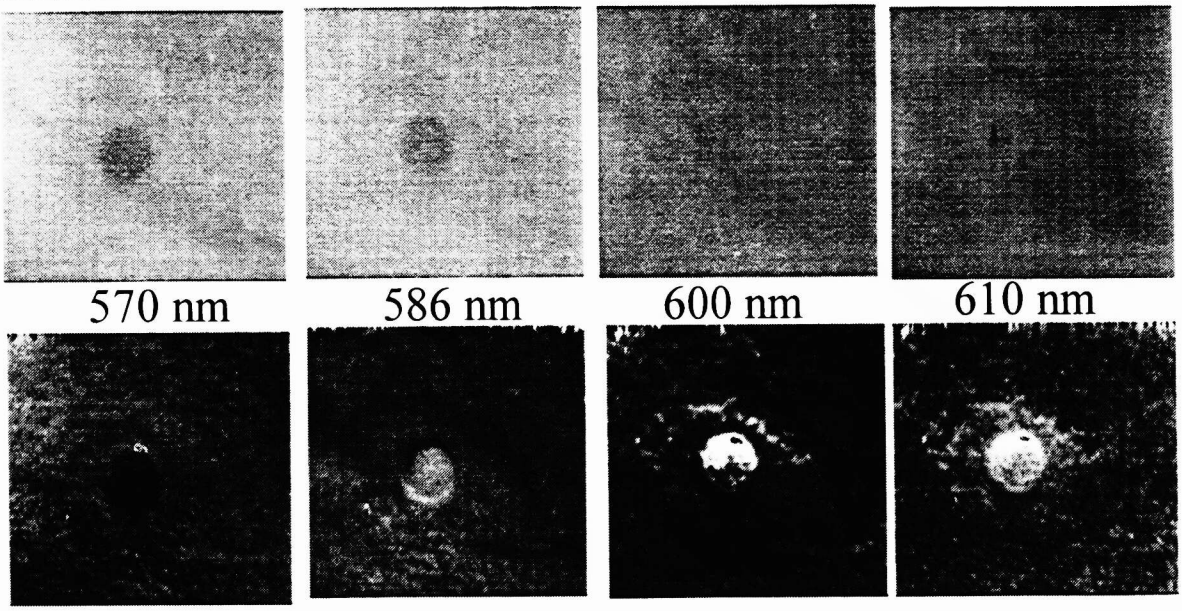

Figure 6 — Hyperspectral Imagery of a Suction Blister.

3829-16